Bi-level and multi-objective optimization of renewable energy sources and storage planning to support existing overloaded electricity grids

Sara Fakih, Mohamed Tahar Mabrouk, Mireille Batton-Hubert, Bruno Lacarrière

Research paper

Bi-level and multi-objective optimization of renewable energy sources and storage planning to support existing overloaded electricity grids

Sara Fakih [a],[*], Mohamed Tahar Mabrouk [a], Mireille Batton-Hubert [b], Bruno Lacarriere [a]

[a] *IMT Atlantique, Department of Energy Systems and Environment, GEPEA, UMR CNRS, 6144, F-44307, Nantes, France*
[b] *Mines Saint-Etienne, University of Clermont Auvergne, CNRS, UMR 6158 LIMOS, Institut Henri Fayol, F-42023, Saint-Étienne, France*

ARTICLE INFO

ABSTRACT

The paper proposes a bi-level multi-objective optimization model to optimally design and operate renewable energy sources and storage systems in an existing electrical grid with increasing demand. while respecting network constraints based. The bi-level optimization model combines particle swarm optimization (PSO) and dynamic linear AC-optimal power flow (DLOPF). The aim of the bi-objective model is to minimize costs while limiting carbon emissions. PSO sizes and identifies the placement of battery energy storage (BES) systems, and DLOPF locates and sizes RES in a spatial–temporal framework using the Levelized Cost of Energy and Storage. Different scenarios were applied to the IEEE-30 bus system to reveal the behavior of the dynamic network for the different cases, and the associated effect of integrating RES and BES. The model resulted in optimized scenarios in terms of placement and sizing of RES and BES at the lowest cost while considering cost minimization and carbon constraints. This shows how the complexity of the CO_2 constraints requires more RES and BES installations and thus more funds. The maximum CO2 limit achieved is 30%, which has reached the storage limits and increased the overall cost by $15 m.

1. Introduction

There has been considerable expansion and growth of the electrical power system over the past two decades. With the worldwide demand for electricity increasing at the rate of 720 TWh per year (IEA, 2019), global CO_2 emissions from the power sector are also increasing, and in 2021 reached a record 36.3 Gt (Flagship report, 2022). The penetration of RES such as solar and wind is increasing in line with the mounting needs of governments worldwide to achieve their energy independence and emissions reduction targets (Maffei et al., 2014).

When a pathway is established for transforming the global energy sector from fossil-based to zero-carbon sources, it gives rise to energy transition policies (IRENA, 2022). As a result, renewables were responsible for 26.3% of worldwide electricity generation in 2020 (15.8% hydropower, 5.3% wind power, etc.) (Ritchie and Roser, 2020), and this figure is expected to rise to 45% by 2040 (World energy outlook 2019, 2019). However, the installed Energy Storage (ES) capacity needs to be 450 GW by 2050 to reduce global warming by 2 °C (Olabi et al., 2021). The growth of these new intermittent energy sources is causing

increased complication for the existing electrical grids and compounding the problem of stabilizing the power flow (Silva, 2018). RES and ES need to be optimally placed and sized at the planning stage to meet demand and help the electricity grids operate more efficiently (Jorgenson et al., 2022). The problem is to find the optimal combination of RES, fossil fuel and ES technologies while reducing carbon emissions to a minimum and maximizing the profitability of the overall electricity network over a multi-period time frame.

Various electric energy planning approaches for integrating different types of renewables have been investigated in the literature. For sizing photovoltaic (PV) systems, a heuristic approach was used in consideration of the price of electricity (Zebarjadi and Askarzadeh, 2016). In Pereira et al. (2016), the integration of wind farms and hydroelectric plants was studied using a deterministic approach with strict targets for CO_2 reduction. Artificial intelligence methods such as PSO, genetic algorithms (GA) and simulated annealing were compared in Torrent-Fontbona and López (2016) to optimize the location of renewable generation sites. These studies demonstrate that PSO outperforms the other methods. GA was used in a bi-level approach to optimize the sizing and operation of battery energy storage (BES) (Ma et al., 2022) and reduce the total cost via optimal configuration of a hybrid PV/Wind Turbine (WT) system with batteries (Yang et al., 2008). The bi-level optimization approaches are also developed for other

Nomenclature

Variables

P	Active power (MW)
Q	Reactive power (MVAr)
S	Apparent power (MVA)
F	Objective function
D	Storage duration
$\mathcal{C}/\mathcal{I}$	Total operational/investment cost by production
Γ	Total cost by category
A	Installed amount of RES
v	Voltage magnitude
θ	Phase angle
G/B	Real/imaginary part of the admittance matrix
g/b	Conductance/susceptance of a branch
ϵ	Variables added to guarantee voltage positivity
E	Active energy level in the BES
X	Population for PSO
Δ_F	Normalized objective function approximation error between two successive iterations
Δ_{tol}	Tolerance for the objective function approximation error

Parameters

C	Elementary operational cost
I	Elementary investment cost
O	Elementary O&M cost
LT	Lifetime
nl	Lifetime of the overall system
En	CO_2 emissions
Ta	CO_2 emissions constraint (%)
α/β	Storage cost constants for BES investment cost calculation
r	Discount rate of the project
η	Battery efficiency
n	Number of segments needed to linearize branch flow limits
li	Group of lines for the branches' flow limits
ra	Random parameters between 0 and 1
w	Inertia weight in PSO
a	Acceleration in PSO

Indices and sets

$\mathcal{N}$	Set of buses, $i,j \in \mathcal{N}$
$\mathcal{T}$	Set of all times, $t \in \mathcal{T}$
$c/u/s/w$	Indices of buses with CG/VG/PV/WT
k	Iteration number in DLOPF
L	Iteration number in PSO
ll/ul	Lower level/Upper level
inv	Investment
$o\&m$	Operation and maintenance
op	Operational
dx	Particle index in PSO

Upper-scripts

cg/vg	Classic generator/virtual generator
pv/wt	Photovoltaic/wind turbines
b	BES index
l	Load index at a bus
c	Charge index of the storage system
d	Discharge index of the storage system
p/q	Active/reactive power
max	Maximum value for the upper limit
cgT	Total produced by classic generators
inj	Injected at the bus
$best$	Best experience of parameter in PSO

Abbreviations

OPF	Optimal power flow
DLOPF	Dynamic Linearized
AC-OPF	Alternating current-OPF
DC-OPF	Direct current-OPF
PV	Photovoltaic
CG	Classic generator
WT	Wind turbines
$p.u$	Per unit
RES	Renewable energy sources
BES	Battery energy storage
VG	Virtual generator
ES	Energy Storage

applications. Thus, a combination of two-layer GA and simulated annealing is used for public charging station localization of electric vehicles (Li et al., 2022). PSO was applied in Maleki et al. (2016) to determine the optimal size for a hybrid multisource system PV/WT/BES. The most commonly-used AI algorithms in the literature are therefore GA and PSO (Lian et al., 2019), with PSO often preferred for its higher probability and efficiency in achieving the global optima (Alshammari and Asumadu, 2020). These approaches presented suitable solutions for reducing computation time and were easy to implement. However, on the whole they did not take into account power flow optimization or physical network constraints.

A territorial energy plan that aims to increase the level of renewable energy sources via a detailed modeling of the network can use optimal power flow (OPF) methods. The authors in Biswas et al. (2017) incorporated wind and solar power in their OPF solutions, using the differential evolution algorithm. However, OPF was used only to optimize a single point in time; to extend the problem over multiple time periods, a dynamic OPF (DOPF) was proposed in Gill et al. (2014). The optimal dispatch of power generation across a network was resolved using DOPF to satisfy power demand within a given timeframe by modeling 'intertemporal' technologies (energy storage) and effects (e.g., flexible demand, generator ramp rates). Similar studies using DOPF can be found in the literature (Azizipanah-Abarghooee et al., 2016; Chung et al., 2011; Haiyan Chen et al., 2005; Morstyn et al., 2016; Uturbey and Costa, 2003), in which interruptible load is investigated as part of the electricity market. Other works have been based on the multi-period optimization method to help propose the optimal placement and usage of renewables and storage systems (Lamadrid et al., 2011), or the active–reactive power dispatch from energy storage (Gabash and Li, 2012). OPF was used dynamically with renewables in Li et al. (2021), using spatial–temporal graph information to improve the stability of

Table 1
Summary of methods for sizing of hybrid renewables energy systems in recent articles.

Refs.	Components			Modeling of power flow	Network type	Model's goal	Utilized methods
	PV	WT	BES				
Ma et al. (2022)			✔	Active power equilibrium equation	Distribution network	- Sizing SB - Operational cost	Bi-level (GA)
Alshammari and Asumadu (2020)	✔	✔	✔	Active power equilibrium equation	Small rural community	- Sizing - Cost - Emissions	Harmony search/Jaya/PSO
Xu et al. (2020)	✔	✔	✔	Active power equilibrium equation	Power supply	- Configuration - Inv. cost	Multi-objective PSO/Weightless Swarm Algorithm
Arabi-Nowdeh et al. (2021)	✔	✔	✔	Active power equilibrium equation	Distribution network	- Size - Emission - Losses PV angle	Sea Horse Optimization
Sadeghi et al. (2020)	✔	✔	✔	Active power equilibrium equation	Distribution network	- Life cycle cost - Loss of power supply probability	Multi-objective PSO
Amigue et al. (2021)	✔			Active, reactive power flow equations + Voltage	Distribution network	- Optimal placement - Loss	Slime mould algorithms
Ali et al. (2017)	✔	✔		Active, reactive power flow equations	Distribution network	- Optimal sizing	Ant Lion Optimization Algorithm
Khan et al. (2020)	✔	✔		Detailed optimal power flow model		- Optimal cost	Grey Wolf Optimizer + OPF
Li et al. (2021)	✔	✔		Detailed optimal power flow model	Distribution network	- Optimal cost	Deep Reinforcement Learning + OPF
This paper	✔	✔	✔	Detailed optimal power flow model	Transmission or distribution networks	- Optimal placement - Sizing - Cost (Inv. + Operational)	Bi-level (PSO + DLOPF)

the network. In Shaheen et al. (2021b), the OPF was resolved using the Hunger Games Search to minimize generation costs by integrating RES. For the same purpose, the authors of Shaheen et al. (2021a) used Heap's algorithm to arrive at the OPF. Although these research works (Li et al., 2021; Shaheen et al., 2021b,a) present several noteworthy models combining RES with OPF models, none have considered BES devices.

Several works have been based on the application of nonlinear OPF formulations (Gabash and Li, 2012; Lamadrid et al., 2011; Uturbey and Costa, 2003), however, these approaches are time-consuming and do not guarantee the global optimum will be achieved. To overcome this difficulty, linear OPF formulations allow the use of linear programming (LP) methods (e.g. the simplex algorithm Bartels and Golub, 1969; Smale, 1983). Kargarian et al. (2018) used this strategy but they used DC-OPF for their dynamic smart electric grid study, which is only applicable in certain circumstances.

BES operations and planning have attracted widespread research attention among researchers (Ma et al., 2022). A stochastic analysis framework was used to determine BES capacity in Bayram et al. (2017), and a cost–benefit analysis was carried out to address the issue of BES capacity sizing. In terms of operational strategy, a centralized energy management system to dispatch PVs and BESs was studied in AlSkaif et al. (2017). An overview of the research on the optimization objectives and requirements of the BES system is presented in Hannan et al. (2021). Based on this overview and on previous works (AlSkaif et al., 2017; Bayram et al., 2017), power flow is scarcely considered and applied primarily to distribution networks. A few works have addressed the transmission network with RES and BES planning; in Li and Li (2021) for example, a combination of GA for component sizing and Mixed-Integer Linear Programming (MILP) for the operation model was used for probabilistic sizing of a low-carbon-emission power supply system. This model is only applicable with high

voltage direct current. In Keck et al. (2022), the network cost was not considered in relation to the optimization issue, and a novel parallel investigation with a near-optimal LP and heuristic optimization approach was carried out on a countrywide scale to estimate the mix for future power generation. It was demonstrated that substantial simplification is required for the LP to be solvable and leads to an overly optimistic installed capacity and cost. The heuristic approach showed a significant advantage in terms of performance, requiring only 3% of the near-optimal runtime and a fraction of the calculation iterations. Bi-level approaches are widely performed in literature and the linearization techniques are validated to reduce the computational time burden. In García-Muñoz et al. (2021), the proposed approach combines GA algorithm and AC-OPF to optimally locate and size RES and BES into distribution network. Another two-stage bi-level approach is detailed in Maiz et al. (2022) for the expansion planning of virtual power plant, a linearization technique is applied also. However, the BES design is rarely based on factors influencing the storage investment cost (e.g., storage duration and power), the cost depreciation rate is not considered in addition to the environmental effect. In brief, Table 1 presents a comparison between different articles in the literature with the present paper regarding the designed technologies (PV, WT or BES), modeling of power flow, network type, model's goal in addition to the utilized methods for the design and operation.

Motivated by these discussions, the aim of the present study is to develop a new bi-level PSO-DLOPF using both heuristic and linear OPF approaches for optimal integration of RES and BES to minimize the total energy cost, taking into consideration various constraints such as existing network constraints, the installable PV surfaces available in each zone, the maximum number of BES systems, and the different carbon emissions constraints. In the upper level, a PSO algorithm was used to locate and size a limited BES to minimize the global cost. In the lower level, a DLOPF

optimization algorithm was calculated for minimization of total investment & operational costs while achieving a certain carbon emissions level.

The proposed approach is adapted for energy planning by:

(1) Transforming the model to a dynamic model
(2) Adding RES systems
(3) Adding BES model
(4) Adding Virtual generators to guarantee a mathematical solution at each time step
(5) Adding a "typical days selection step" to ensure that the simulation is representative of the entire year operation.

The paper is structured as follows: Section 2 presents the methodology, including planning strategies, grid description, the DLOPF model and the optimization algorithm. Section 3 presents the formulation of the problem and the solution. Section 4 gives the results and analysis of the simulation, followed by the conclusion in Section 5.

2. Methodology and models

2.1. Methodology

RES and BES could be installed in transmission networks to tackle the increase in energy requirements and/or to raise the proportion of renewable energy in the system. A methodology was developed to optimize the size and location of RES and BES in transmission networks to generate sufficient power to meet the higher demand but remain within existing grid constraints. The overall structure for the proposed approach PSO-DLOPF is presented in Fig. 1. In a bi-level structure, the upper-level (left side of Fig. 1) of the model first optimized BES placement and size using an iterative method to minimize an objective function using the PSO. This calculation was based on results from a lower-level (right side of Fig. 1) model which optimized the placement of renewable generation units and energy production and storage dispatch using DLOPF, then transferred the results to the upper-level. The upper-level then updated the placement and size of the batteries and transferred them back to the lower level. The process was repeated until the end criteria were achieved and the optimum arrived at.

The overall structure of the proposed PSO-DLOPF model shown in Fig. 1 is detailed as follows:

Step 1. Set iteration number for the upper level, collect input parameters boundaries, initialize population X as the solution of the upper level and obtain BES location, duration and power from X. Transfer X to the lower level.

Step 2. Collect relevant data, input grid parameters and load data. Initialize voltage (V_0) and voltage angle (θ_0) values. Transmit BES design information X to lower level as known parameters. Calculate the lower-level objective function (F_{ll}) for the first iteration.

Step 3. Update lower-level iteration by updating V_k and θ_k according to the results of the first iteration. Recalculate F_{ll}.

Step 4. Evaluate the termination condition to determine whether a stopping criterion is achieved. If so, the recorded optimal value is passed back to the upper level to calculate the upper-level objective function value.

Step 5. Increase the number of iterations L = L + 1. Update the upper-level population X and transfer the updated population from upper to lower level to repeat steps 2–4.

Step 6. Increase the number of iterations L = L + 1. If the stopping criterion is met, exit the loop to stop the iteration.

Step 7. Transfer X_{best} values to the lower level to obtain the optimal values for the proposed design.

2.2. Upper-level model: optimal placement and planning of BES

2.2.1. Definition of optimization problem

The upper-level model finds the optimal placement and size for the BES by optimizing the levelized cost of energy (LCOE), which includes total investment, production, maintenance, and operational (O&M) costs.

The LCOE is defined as the price at which the generated electricity should be sold for the system to break even at the end of its lifetime (Walter Short et al., 1995). The upper level objective function F_{ul} is the LCOE of the system, including BES defined as the sum of two terms: first, the actualized cost of BES and second the optimal levelized cost of RES installation, maintenance and energy production from classic energy sources (F_{ll}). The latter is a result of the lower-level optimization issue where optimal placement and sizing of RES and optimal energy production and storage dispatch is carried out. This is expressed in Eq. (1) (*The optimization variables appear in* **bold** *below.*)

$$min\, F_{ul} = min \frac{\mathfrak{I}^b.(\frac{nl}{LT^b})}{\sum_{\boldsymbol{i}=1}^{I} \sum_{t=1}^{\mathfrak{T}} \frac{P_{\boldsymbol{i},t}^l}{(1+r)^t}} + min(F_{ll}) \tag{1}$$

where $\mathfrak{I}^b$ is the investment cost of the batteries which is actualized using the discount project rate (r). The ratio between the lifetime of the overall system (nl) by the BES lifetime (LT^b) is used to account for the replacement cost of the batteries during the lifespan of the project.

Eq. (2) expresses the investment cost of BES. The cost of batteries, as reported in the literature, depends on maximum discharge power $\boldsymbol{P^b}$ and discharge duration $\boldsymbol{D}$ (Cole et al., 2021). The battery investment cost is therefore modeled as a specific capital cost in ($/kW) multiplied by the battery's maximum power $\boldsymbol{P^b}$. The specific cost is modeled as a linear function of the battery's duration. The slope α and intercept β of this function are determined by linear regression of the specific capital costs of lithium-ion systems for typical durations (Cole et al., 2021). The values of $\boldsymbol{P_{ib}^b}$ and $\boldsymbol{D_{ib}}$ are limited by the upper bounds of the existing battery power $\left(P_{ib}^{b^{max}}\right)$ and maximum storage duration D_{ib}^{max} given by Eq. (3). $\boldsymbol{i^b}$ belongs to a continuous interval with all bus indices (from 1 to $\mathbb{N}$) to give the possibility of installation on all nodes. To design a battery, the maximum battery energy $E_{ib}^{\boldsymbol{b}}$ is calculated by Eq. (4) in terms of $\boldsymbol{D_{ib}}$ and $\boldsymbol{P_{ib}^b}$ for each BES located at node $\boldsymbol{i^b}$.

$$\mathfrak{I}^b = \sum_{\boldsymbol{i^b}=1}^{\mathbb{N}} (\alpha.\boldsymbol{D_{ib}} + \beta).\boldsymbol{P_{ib}^b} \tag{2}$$

$$S.t \begin{cases} 0 \le \boldsymbol{P_{ib}^b} \le P_{ib}^{b^{max}} \\ 1 \le \boldsymbol{i^b} \le \mathbb{N} \\ 0 \le \boldsymbol{D_{ib}} \le D_{ib}^{max} \end{cases} \tag{3}$$

$$E_{ib}^{\boldsymbol{b^{max}}} = \boldsymbol{D_{ib}}.\boldsymbol{P_{ib}^{b^{max}}} \tag{4}$$

The optimization variables in the upper level are $\boldsymbol{D_{ib}}$, $\boldsymbol{P_{ib}^b}$ and $\boldsymbol{i^b}$.

2.2.2. Particle Swarm Optimization (PSO) model

PSO is used because the upper-level model contains nonlinear equations describing the nonlinear battery costs (2) (Maleki et al., 2016). PSO is a population-based metaheuristic algorithm to attempt identification of the global solution to an optimization problem by simulating the social behavior of animals, such as bird grouping. In the PSO algorithm, each feasible solution is a particle and is specified by a vector containing all the variables. The particles 'fly' through the N-dimensional domain space of the function to be minimized. The state of each particle is represented
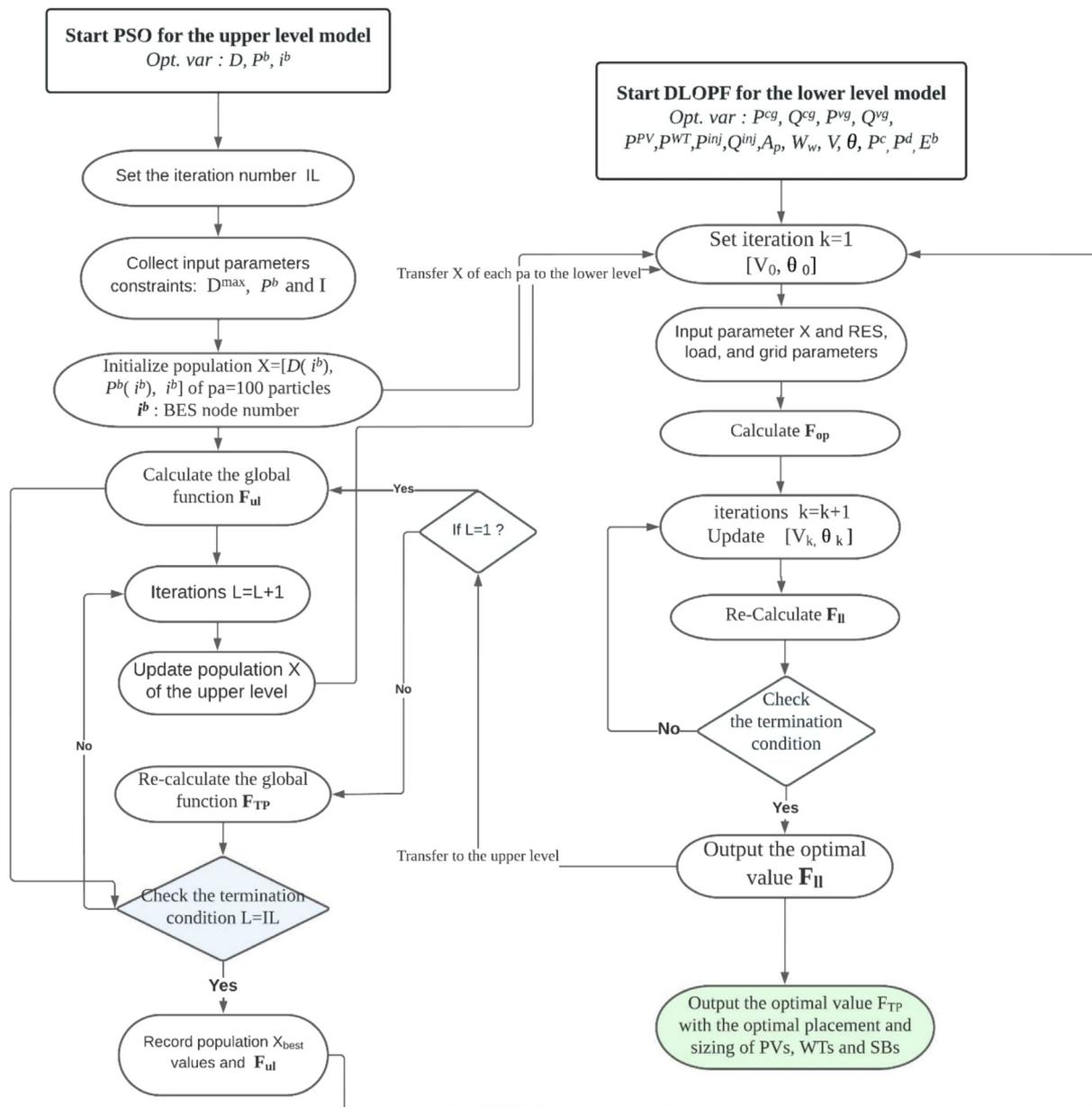
Fig. 1. Flowchart for the proposed bi-level PSO-DLOPF solution.

by its position $xe_d = (xe_{d1}, xe_{d2}, \ldots, xe_{dN})$ and velocity $ve_d = (ve_{d1}, ve_{d2}, \ldots, ve_{dN})$. The states are then updated using Eqs. (5) and (6).

$$ve_{dx}^{L+1} = w^L.ve_{dx}^L + a_1.ra_1^L.\left(pe_{best_{dx}}^L - xe_{dx}^L\right) + a_2.ra_2^L.(ge_{best}^L - xe_{dx}^L)$$
(5)

$$xe_{dx}^{L+1} = xe_{dx}^L + v_{dx}^{L+1}$$
(6)

The velocity update Eq. (5) contains three key parameters. These parameters are the momentum component (the acceleration constant a_1) which is used to control how far the particle gets towards its personal best position. The second is the inertial constant (w) which controls how long the particle remembers its previous velocity. The third is the social component (the acceleration constant a_2), which draws the particle toward the best position in the swarm. ra_1 and ra_2 are random variables between 0 and 1. The inertia weight w starts from an initial value of $w_0 \geq 0$ and decreases throughout the iterations $w^{L+1} = \mu \times w^L$. pe_{best}^L (best experience alone) is the best position achieved so far

by particle dx and its k times, and ge_{best}^L (best experience of group) is the best position achieved by the swarm in its optimal position (Maleki et al., 2016).

2.3. Lower-level optimization: RES planning

2.3.1. Definition of the optimization problem

The objective in the lower-level optimization model is to minimize the LCOE of the production system. This corresponds to the LCOE of the whole system, not including BES costs. In the lower level, four types of generators are present, the RES such as PVs and WTs, the classic generators (CGs) and the virtual generators (VGs). VGs are the new elements supposed to be presented at all buses with a generation cost significantly higher than real generators (CG, PV, WT) aiming to guarantee a feasible solution at each time step. The optimization is carried out for three typical durations from one full year. The objective function is presented by Eq. (7). This function is the levelized cost of energy that combines investment, operational, O&M costs to cover the system's

lifetime aiming to estimate the actualized cost per unit of energy produced. In this Eq. (7), Γ_{inv} [detailed in Eq. (8)] is the sum of the investment costs for the WTs ($\mathcal{J}^{wt}$) and PVs ($\mathcal{J}^{pv}$). Γ_{op} is the total operational cost represented by Eq. (9), where the production cost of classic generators (CGs) ($\mathcal{C}^{cg}$) and virtual generators (VGs) ($\mathcal{C}^{vg}$) is minimized. As solar and wind power are clean energy sources, their corresponding operational costs (C^{wt}, C^{pv}) are zero. The total actualized operational cost for CGs ($\mathcal{C}^{cg}$) is expressed by Eq. (10), where the sum of the active ($\boldsymbol{P^{cg}}$) and reactive ($\boldsymbol{Q^{cg}}$) power produced is multiplied by the corresponding costs ($C^{cg,p}$ for active and $C^{cg,q}$ for reactive). As with Eqs. (10), (11) gives the virtual generation cost (C^{vg}). In each bus, the generation costs of the virtual generators are significantly higher than those of other generators (both $C^{vg,p}$ and $C^{vg,q}$) to produce a feasible solution and serve as an indicator for the production deficit on the corresponding bus. The total operational costs of WTs ($\mathcal{C}^{wt}$) and PVs ($\mathcal{C}^{pv}$) are given respectively by Eqs. (12) and (13). In terms of investment costs, the installation area for PVs is the optimization variable $\boldsymbol{A^{pv}}$, which is multiplied by the investment cost (I^{pv}) [Eq. (14)]. $\boldsymbol{A^{pv}}$ is bounded by the available surface area for installing PVs ($\boldsymbol{A^{pv^{max}}}$) [Eq. (21)]. The continuous variable $\boldsymbol{A^{wt}}$ gives the ratio of exploitable local wind energy. $\boldsymbol{A^{wt}}$ is bounded by $\boldsymbol{A^{wt^{max}}}$, which corresponds to the maximum exploitable power based on unitary WT production, WT_t. $\boldsymbol{A^{wt}}$ is indirectly defined by the available surface area of the bus in question, multiplied by the investment cost (I^{wt}) Eq. (15).

$\Gamma_{o\&m}$ in Eq. (16) is dependent on the WTs and PVs installed and their O&M costs (O^{wt}, O^{pv}) and on existing CG maintenance costs (O^{cg}). All these variables are bounded as shown in (21). Hourly PV and WT production ($\boldsymbol{P^{pv}_{s,t}}$ and $\boldsymbol{P^{wt}_{w,t}}$) is bounded by time-dependent maximum power ($P^{pv^{max}}_{s,t}$ and $P^{wt^{max}}_{w,t}$), as detailed in Eqs. (17) and (18). These maximum powers are calculated using Eqs. (19) and (20), where PV_t and WT_t are respectively the unitary PV and WT power production.

$$\min F_{ll} = \min \frac{(\Gamma_{op} + \Gamma_{o\&m}) + \Gamma_{inv}}{\sum_{i=1}^{\mathcal{N}} \sum_{t=1}^{\mathcal{T}} \frac{P^l_{i,t}}{(1+r)^t}} \tag{7}$$

$$\Gamma_{inv} = \mathcal{J}^{wt} + \mathcal{J}^{pv} \tag{8}$$

$$\Gamma_{op} = \mathcal{C}^{cg} + \mathcal{C}^{vg} + \mathcal{C}^{wt} + \mathcal{C}^{pv} \tag{9}$$

$$\mathcal{C}^{cg} = \sum_{t=1}^{\mathcal{T}} \sum_{c=1}^{\mathcal{N}^{cg}} \frac{C^{cg,p} . \boldsymbol{P^{cg}_{c,t}} + C^{cg,q} . \boldsymbol{Q^{cg}_{c,t}}}{(1+r)^t} \tag{10}$$

$$\mathcal{C}^{vg} = \sum_{t=1}^{\mathcal{T}} \sum_{i=1}^{\mathcal{N}^{vg}} \frac{(C^{vg,p} . \boldsymbol{P^{vg}_{i,t}} + C^{vg,q} . \boldsymbol{Q^{vg}_{i,t}})}{(1+r)^t} \tag{11}$$

$$\mathcal{C}^{wt} = \sum_{t=1}^{\mathcal{T}} \sum_{w=1}^{\mathcal{N}^{wt}} \frac{C^{wt} . \boldsymbol{P^{wt}_{w,t}}}{(1+r)^t} \tag{12}$$

$$\mathcal{C}^{pv} = \sum_{t=1}^{\mathcal{T}} \sum_{s=1}^{\mathcal{N}^{pv}} \frac{C^{pv} . \boldsymbol{P^{pv}_{s,t}}}{(1+r)^t} \tag{13}$$

$$\mathcal{J}^{pv} = \sum_{s=1}^{\mathcal{N}^{pv}} I^{pv} . \boldsymbol{A^{pv}_s} \tag{14}$$

$$\mathcal{J}^{wt} = \sum_{w=1}^{\mathcal{N}^{wt}} I^{wt} . \boldsymbol{A^{wt}_w} \tag{15}$$

$$\Gamma_{o\&m} = \sum_{i=1}^{\mathcal{T}} (O^{pv} . \boldsymbol{A^{pv}} + O^{wt} . \boldsymbol{A^{wt}} + O^{cg} . \boldsymbol{P^{cgT}}) \tag{16}$$

$$0 \leq \boldsymbol{P^{pv}_{s,t}} \leq P^{pv^{max}}_{s,t} \qquad \forall p \in [0, \mathcal{N}^{pv}] \tag{17}$$

$$0 \leq \boldsymbol{P^{wt}_{w,t}} \leq P^{wt^{max}}_{w,t} \qquad \forall w \in [0, \mathcal{N}^{wt}] \tag{18}$$

$$P^{pv^{max}}_{s,t} = \boldsymbol{A^{pv}_s} . PV_t \tag{19}$$

$$P^{wt^{max}}_{w,t} = \boldsymbol{A^{wt}_w} . WT_t \tag{20}$$

$$S.t \begin{cases} 0 \leq \boldsymbol{P^{cg}_{c,t}} \leq P^{cg^{max}}_c & \forall c \in [0, \mathcal{N}^{cg}] \\ 0 \leq \boldsymbol{P^{vg}_{i,t}} \leq P^{vg^{max}}_i & \forall i \in [0, \mathcal{N}^{vg}] \\ 0 \leq \boldsymbol{Q^{cg}_{c,t}} \leq Q^{cg^{max}}_c & \forall c \in [0, \mathcal{N}^{cg}] \\ 0 \leq \boldsymbol{Q^{vg}_{i,t}} \leq Q^{vg^{max}}_i & \forall i \in [0, \mathcal{N}^{vg}] \\ 0 \leq \boldsymbol{A^{pv}_s} \leq A^{pv^{max}}_s & \forall s \in [0, \mathcal{N}^{pv}] \\ 0 \leq \boldsymbol{A^{wt}_w} \leq A^{wt^{max}}_w & \forall w \in [0, \mathcal{N}^{wt}] \end{cases} \tag{21}$$

$$\sum_{t=1}^{\mathcal{T}} \sum_{i=1}^{\mathcal{N}} En^{cg} . \boldsymbol{P^{cg}_{c,t}} \leq En^{cgT} . Ta \tag{22}$$

In electricity generation, only CGs are considered to emit CO_2 since other power generators (PVs and WTs) are zero-emissions; the minimization of total CO_2 emissions is the objective when designing RES and BES. Following the ε-constraint method (Mavromatidis et al., 2018), a constraint setting using an upper limit for CO_2 emissions, referred to as an emissions constraint (Ta), is expressed in Eq. (22). The Ta can be selected by the system designer and varied to obtain various designs that achieve different carbon performances. The CO_2 emissions are calculated over selected periods in which 100% of power is extracted from classic generators to fix the value at En^{cgT}. The CO_2 emissions are calculated by the product of $\boldsymbol{P^{cg}_{c,t}}$ and En^{cg}, which is the carbon emitted by 1 MWh of classic energy.

2.3.2. Optimal power flow model

The linear OPF algorithm optimizes generator dispatch and determines the optimal value for the variables identified at each bus of the network by linearizing the AC OPF equations. These variables include active and reactive power input, voltage, phase angles and storage levels in the battery. Also included are the active and reactive power flows that circulate in each branch between two nodes subject to the loading constraints of the network branches. The optimization process is based on *Yang et al.*'s methodology (Yang et al., 2016), for which an iterative optimization approach was used. A linear optimization process is first carried out around an approximation. Following resolution, a new operating point is found and used to update this approximation. This procedure is repeated iteratively until convergence is achieved. The approach is upgraded in the present work by adding equations for virtual generators and energy storage in the desired buses to create a dynamic simulation of the network and storage devices (Fakih et al., 2022). The OPF model can therefore be summarized as follows:

2.3.2.1. OPF equality constraints.

Energy balance in buses

To guarantee equilibrium between production and demand at each bus, the injected power must be equal to the consumed power. Eq. (23) expresses the active power equilibrium concept for each bus, the parameters on the left being the active power extracted from the classic (P^{cg}_i) and virtual (P^{vg}_i) generators, the power produced from both PVs (P^{pv}_i) and WTs (P^{wt}_i), and the discharging power variable (P^d_i). The elements on the right are the active power demand (P^l_i), the power P^{inj}_i injected into the network at bus $i/i \in \mathcal{N}$ (where $\mathcal{N}$: set of buses), and the charging power variable of the battery (P^c_i). With reactive power, the same equilibrium concept is expressed by Eq. (24) which does not take into consideration the reactive power variable of the battery (battery power factor equal to 1). Since this model is dynamic, all the optimization variables are time-dependent. For the sake

of simplicity, the time-dependence notation is dropped in all equations except for battery equilibrium (46).

$$\sum_{i \in \mathcal{N}} P_i^{cg} + P_i^{pv} + P_i^{wt} + P_i^{vg} + P_i^{d} = P_i^{l} + P_i^{inj} + P_i^{c} \qquad i \in \mathcal{N} \quad (23)$$

$$\sum_{i \in \mathcal{N}} Q_i^{cg} + Q_i^{vg} = Q_i^{l} + Q_i^{inj} \qquad i \in \mathcal{N} \quad (24)$$

Active and reactive power injection

Power flow equations are usually expressed in their general nonlinear form as follows:

$$P_i = \sum_{j=1}^{\mathcal{N}} (v_i v_j G_{ij} cos\theta_{ij} + v_i v_j B_{ij} sin\theta_{ij}) \quad (25)$$

$$Q_i = -\sum_{j=1}^{\mathcal{N}} (v_i v_j B_{ij} cos\theta_{ij} - v_i v_j G_{ij} sin\theta_{ij}) \quad (26)$$

where P_i and Q_i are respectively the active and reactive power injected into the network at bus i, and G_{ij} and B_{ij} are the real and imaginary parts of the network's admittance matrix. θ and v are respectively the voltage angle and the voltage at each bus.

These equations are linearized, given the initial estimated values for voltage and voltage angle (v_i^k, θ_i^k) and updated at each iteration k ($v_i^0 = 1$, $\theta_i^0 = 0$). For the linearization procedure, θ and v^2 are considered independent variables and the cosine and sine functions are linearized using their first-order Taylor series expansion as follows:

$$sin\theta_{ij} \approx S_{ij,k}^1 \theta_{ij} + S_{ij,k}^0 \quad (27)$$

$$cos\theta_{ij} \approx h_{ij,k}^1 \theta_{ij} + h_{ij,k}^0 \quad (28)$$

$$s_{ij,k}^1 = \cos\theta_{ij,k}, \qquad s_{ij,k}^0 = \sin\theta_{ij,k} - \theta_{ij,k}.cos\theta_{ij,k} \quad (29)$$

$$h_{ij,k}^1 = -\sin\theta_{ij,k}, \qquad h_{ij,k}^0 = \cos\theta_{ij,k} + \theta_{ij,k}.sin\theta_{ij,k} \quad (30)$$

The following mathematical transformation (31) is then used to extract a linear expression for an accurate representation of $v_i.v_j$.

$$v_i.v_j = \frac{1}{2}\left(v_i^2 + v_j^2 - \left(v_i - v_j\right)^2\right) = \frac{v_i^2 - v_j^2}{2} - \frac{v_{ij}^2}{2} \quad (31)$$

$$with \quad v_{ij} = v_i - v_j$$

v_{ij}^2 is then linearized in (32) to define a new term $v_{ij,L}^s$:

$$v_{ij}^2 \cong 2v_{ij,k}.v_{ij} - v_{ij,k}^2 \cong 2\frac{v_{i,k} - v_{j,k}}{v_{i,k} + v_{j,k}}\left(v_i^2 - v_j^2\right) - v_{ij,k}^2 = v_{ij,L}^s \quad (32)$$

The linear approximation given in (32) can lead to negative values, which contradicts the fact that v_{ij}^2 determines the influence of the difference in voltage magnitudes on the losses. To ensure that the v_{ij}^2, ϵ_{ij} values are positive, variables are added and the new inequality constraints added to the optimization problem (Yang et al., 2016):

$$2\frac{v_{i,k} - v_{j,k}}{v_{i,k} + v_{j,k}}\left(v_i^2 - v_j^2\right) - v_{ij,k}^2 + \epsilon_{ij} \geq 0 \quad with \ \epsilon_{ij} \geq 0 \quad (33)$$

ϵ_{ij} are penalized (multiplied by very high coefficients) as an objective function to ensure they are close to zero.

Injected active and reactive powers are then calculated around a known solution (v_i^k, θ_i^k) using linearized Eqs. (34) and (35):

$$P_i = \sum_{j=1}^{\mathcal{N}}\left[G_{ij,k}^p \frac{v_i^2 + v_j^2}{2} + B_{ij,k}^p\left(\theta_{ij} - \theta_{ij,k}\right) - G_{ij,k}^p \frac{v_{ij,L}^s}{2}\right] \qquad i \in \mathcal{N} \quad (34)$$

$$Q_i = \sum_{j=1}^{\mathcal{N}}\left[-B_{ij,k}^q \frac{v_i^2 + v_j^2}{2} + G_{ij,k}^q\left(\theta_{ij} - \theta_{ij,k}\right) - B_{ij,k}^q \frac{v_{ij,L}^s}{2}\right] \qquad i \in \mathcal{N} \quad (35)$$

where:

$$G_{ij,k}^p = \left(G_{ij}.h_{ij,k}^0 + B_{ij}.s_{ij,k}^0\right) + \left(G_{ij}.h_{ij,k}^1 + B_{ij}.s_{ij,k}^1\right)\theta_{ij,k} \quad (36)$$

$$B_{ij,k}^p = \left(G_{ij}.h_{ij,k}^1 + B_{ij}.s_{ij,k}^1\right)v_{i,k}.v_{j,k} \quad (37)$$

$$B_{ij,k}^q = -\left(G_{ij}.s_{ij,k}^0 + B_{ij}.h_{ij,k}^0\right) - \left(G_{ij}.s_{ij,k}^1 - B_{ij}.h_{ij,k}^1\right)\theta_{ij,k} \quad (38)$$

$$G_{ij,k}^q = \left(G_{ij}.s_{ij,k}^1 - B_{ij}.h_{ij,k}^1\right)v_{i,k}.v_{j,k} \quad (39)$$

Branch flows:

Using the same approximations as for power injections, the linear equations for branch flows are deduced in (40) and (41) and the parameters calculated in (42) to (45).

The active and reactive power flows in the branches can be calculated to facilitate the addition of a maximal apparent power constraint to the branches:

$$P_{ij} = g_{ij}.v_i^2 - g_{ij,k}^p.\frac{v_i^2 + v_j^2}{2} - b_{ij,k}^p\left(\theta_{ij} - \theta_{ij,k}\right) + g_{ij,k}^p\frac{v_{ij,L}^s}{2} \quad (40)$$

$$Q_{ij} = -b_{ij}.v_i^2 + b_{ij,k}^q.\frac{v_i^2 + v_j^2}{2} + g_{ij,k}^q\left(\theta_{ij} - \theta_{ij,k}\right) + b_{ij,k}^p\frac{v_{ij,L}^s}{2} \quad (41)$$

where:

$$g_{ij,k}^p = \left(g_{ij}.h_{ij,k}^0 + b_{ij}.s_{ij,k}^0\right) + \left(g_{ij}.h_{ij,k}^1 + b_{ij}.s_{ij,k}^1\right)\theta_{ij,k} \quad (42)$$

$$b_{ij,k}^p = \left(g_{ij}.h_{ij,k}^1 + b_{ij}.s_{ij,k}^1\right)v_{i,k}.v_{j,k} \quad (43)$$

$$b_{ij,k}^q = -\left(g_{ij}.s_{ij,k}^0 + b_{ij}.h_{ij,k}^0\right) - \left(g_{ij}.s_{ij,k}^1 - b_{ij}.h_{ij,k}^1\right)\theta_{ij,k} \quad (44)$$

$$g_{ij,k}^q = \left(g_{ij}.s_{ij,k}^1 - b_{ij}.h_{ij,k}^1\right)v_{i,k}.v_{j,k} \quad (45)$$

Battery State of Charge (SoC):

The active energy level in the battery at time t $(E_{i,t}^b)$ is calculated using Eq. (46), where the energy stored in the battery is updated at each time step based on the energy level from the previous time step $(E_{i,t-1}^b)$ or the power stored $P_{i,t}^c$, or is discharged $P_{i,t}^d$ from the battery in the current time step. η^c and η^d represent the charge and discharge efficiencies respectively.

$$E_{i,t}^b = E_{i,t-1}^b + \eta^c P_{i,t}^c - P_{i,t}^d/\eta^d \quad (46)$$

2.3.2.2. OPF inequality constraints.

Branch flows limit

The inequality constraints are based on the limits of the apparent power flowing in the branches of the grid. A quadratic Eq. (47) limits the apparent allowable power (S_{ij}^{max}) by a circle area to avoid overloading, using the active and reactive powers P_{ij} and Q_{ij} flowing between two buses (i and j).

$$(P_{ij,k})^2 + (Q_{ij,k})^2 \leq S_{ij}^{2max} \qquad i,j \in \mathcal{N} \quad (47)$$

To linearize this equation, the circle area can be approximated by a polygon region formed by a group of lines li, given in the Eq. (48). The nonlinear equation is thereby transformed into n linear equations. With this approach, a higher number of sides 'n' leads to a more accurate solution, but with a greater computational burden (Akbari and Tavakoli Bina, 2016).

$$\left(\sin\left(\frac{360 * li}{n}\right) - \sin\left(\frac{360}{n}(li-1)\right)\right)Q_{ij}$$
$$-\left(\cos\left(\frac{360 * li}{n}\right) - \cos\left(\frac{360}{n}(li-1)\right)\right)P_{ij}$$
$$-S_{ij}^{max} * \sin\left(\frac{360}{n}\right) \leq 0 \quad (48)$$

2.3.3. DLOPF algorithm

Development of the DLOPF model is based on an LOPF formulation adapted for the use of transmission or distribution networks. The load profiles are used as input data covering the
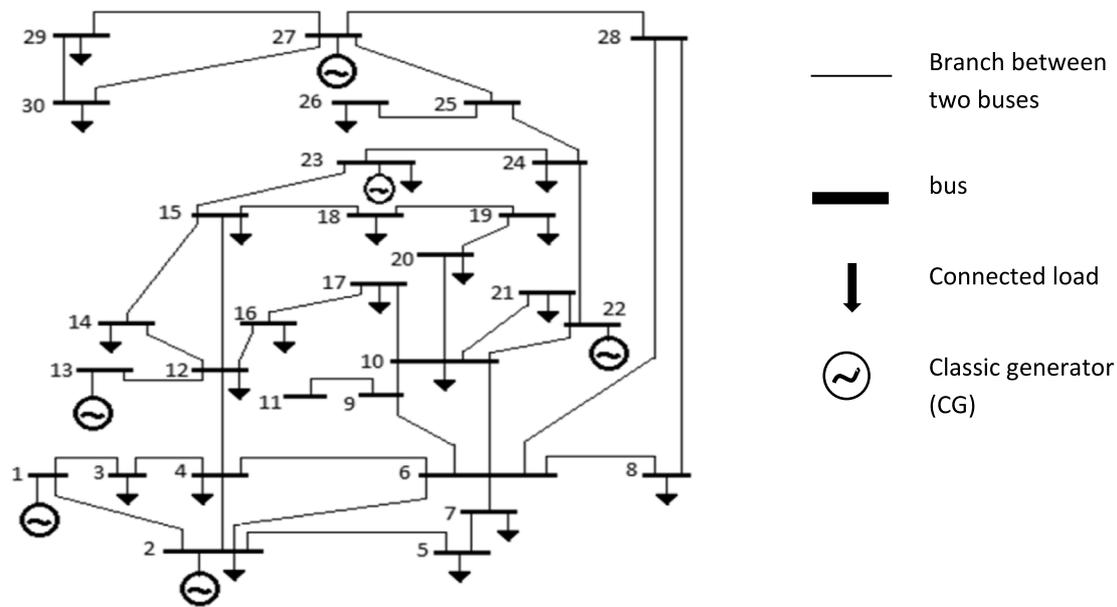
Fig. 2. IEEE 30 bus electricity system for numerical simulation (base network).

targeted period. Modeling of the network architecture and constraints is required, along with a definition of the boundaries (*lb* and *ub*) of the output solution. The objective function uses real values and virtual power is well penalized.

All these conditions must be in place to solve the problem with a single optimization procedure, by summarizing all time periods to achieve an optimal overall solution. Given a flat start point $(v_i^0 = 1 p.u., \theta_i^0 = 0)$, the LOPF model was built and resolved, leading to new voltage and angle values which were used to update the estimate. The number of iterations was not fixed; the process was repeated until the stop criterion was reached. This criterion is defined as the deviation of objective function between two successive iterations ($k-1$ and k) with approximations, using the following equation:

$$\Delta_F = \left| \frac{F^k - F^{k-1}}{F^k} \right| \qquad k \in [1, 2, ..] \tag{49}$$

When $\Delta_F < \Delta_{tol}$, the stop criterion is satisfied.

The optimization variables at the lower level can therefore be categorized as:

1. Design variables: $\boldsymbol{A^{pv}}, \boldsymbol{A^{wt}}$
2. Operation variables: $\boldsymbol{P^{pv}}, \boldsymbol{P^{wt}}, \boldsymbol{P^{cg}}, \boldsymbol{P^{vg}}, \boldsymbol{Q^{cg}}, \boldsymbol{Q^{vg}}, \boldsymbol{V}, \boldsymbol{\theta}, \boldsymbol{P^c}, \boldsymbol{P^d}, \boldsymbol{E^b}$

3. Case studies

Several case studies are presented below to confirm the effectiveness of the model for integrating RES and BES into transmission networks, with the dual aim of minimizing production costs and reducing CO$_2$ emissions.

In this study, an IEEE-30 bus system (Fig. 2) was used (Kristiansen, 2003). The parameters and compositions are summarized in Table 2. A full description of the system components can be found in Hota and Naik (2016). The system incorporated six generation units – either thermal generators or substations – at buses 1, 2, 13, 22, 23 and 27.

Considering one year of data for electricity demand, wind power, and solar power in hour scale would result in a very big optimization problem and, therefore, a long calculation time. The usual procedure in this case is to refer to days rather than

Table 2
Summary of IEEE-30 bus system.

Item	Quantity	Details
Bus	30	Hota and Naik (2016)
Branch	41	Electrical lines details, resistance and reactance (Hota and Naik, 2016) Maximum transmission capacity = 9.2 MVA
Classic generator (CG) (generator or distribution transformer)	6	Buses: 1, 2, 13, 22, 23 and 27
Connected load	20	59% residential, 19.8% commercial and 21.2% mix
Phase angle	–	Ranges [−0.35; +0.35]
Voltage	–	Ranges [+0.9; +1.1]

the full year. To select the most significant typical days, the total load profile is calculated for one year first. Then, this total profile is sliced into subgroups of 3 consecutive days each (72 continuous hours). This continuation allows visualizing the continuous behavior of the storage systems. One hundred twenty-two different subgroups are obtained. Thus, these subgroups are separated into 3 clusters using k-means clustering that classifies similar time series in the same cluster (here 3: winter, summer and spring). This clustering was based on three different features: the total energy demand of the three days, the maximum power reached and the variance of the power demand in each period. The means (centroids) are calculated for the 3 clusters to select one representative period from each cluster. The calculation of the Euclidean distance between each subgroup and the centroids follows this step. Then the nearest element to the 3 different centroids is selected. The 'selected days' are defined as the days that correspond to the chosen periods. Then, the demand profiles for each individual bus are formed by selecting the 'selected days' through the demand curve of the whole year. These periods are placed for each bus alongside each other (9 days classified 3 by 3 continuously). The total load profile for all buses is shown in Fig. 3 for the typical days selected; these are representative of the dynamics occasioned by seasonal variations (summer: low demand, winter: high demand and mid-season: medium demand), allowing a nine-day period for consideration of storage dynamics.
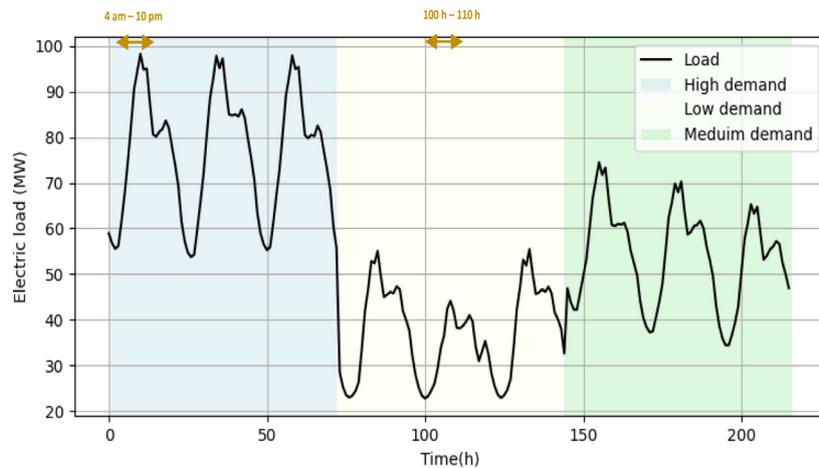
Fig. 3. Total demand for nine typical days from three seasons (high = winter, low = summer, medium = spring) simulated using HOMER Pro software (HOMER Pro, 2022).
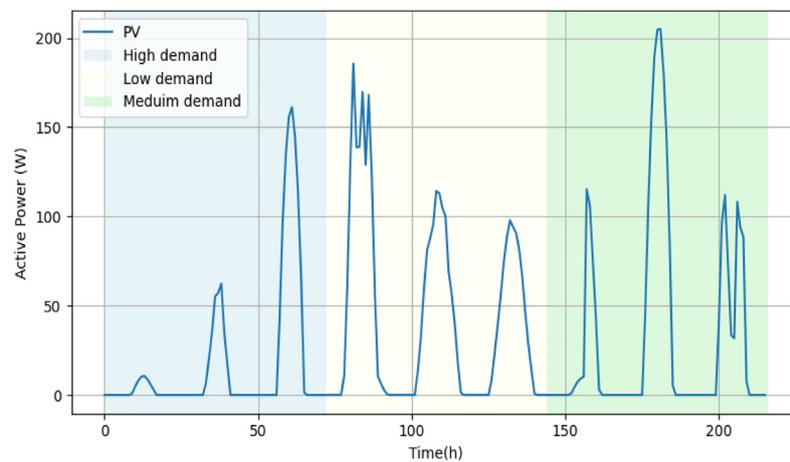

Fig. 4. Profile of one m^2 of PVs for nine typical days from three seasons (high = winter, low = summer, medium = spring) simulated using HelioScope solar design software.

Descriptions

The bus index for the batteries belongs to a continuous interval with boundaries limited by the number of available buses. Thus $i^b \epsilon [1, \mathbb{N}]$ *with* $\mathbb{N} = 30$ *buses*. The values obtained were then rounded to the nearest integer to set the bus index.

Battery duration is limited to 8 h. $D \epsilon [0, 8]$.

Maximum battery power $P^{b^{max}} = 8$ MW.

Maximum installable surface for PV ($A^{pv^{max}}$) 300 000 m^2 each, in buses 4, 9, 10, 12, 20, 26 and 30. The solar resource per unit of surface area at the location (Nantes, France) is given in Fig. 4. This profile should be the same for all buses in this work.

Maximum number of wind turbines allowed per wind farm ($A^{wt^{max}}$) 25, at buses 3,16, 19,21, 25, and 30. The wind power production for 1 MW of rated power based on local wind resources in Nantes is shown in Fig. 5. This profile should be the same for all buses in this work.

All existing buses were considered as candidates for installation of 4 BES. Storage cost constants are presented in Eq. (2), values: $\alpha = 100\,000$, $\beta = 200\,000$ (calculation based on lithium-ion capital cost interpolation for 2, 4 and 6 h in Cole et al., 2021).

The operational and investment costs of the different production sources are given in Table 3.

Fig. 4 shows the PV profile simulated using HelioScope solar design software (HelioScope | Commercial Solar Software, 2022)

based on the coordinates of the intended location for the system (Nantes, France).

Fig. 5 shows the simulated production profile for a wind turbine (WT). The annual WT profile was simulated using HOMER Pro software (HOMER Pro, 2022) for the case-study location in Nantes, selecting the type and number of turbines. The profile was then normalized.

4. Results and discussion

4.1. Validation of LOPF

The linearized model (LOPF) was validated using the Matpower benchmark reference model (Kristiansen, 2003) to confirm its accuracy; the specifications as defined in Matpower for the 'Case30' (Gonzalez-Longatt, 2010) and illustrated by Fig. 2 were used. Optimization with the LOPF was first carried out on the network and the resulting active and reactive power and voltage values were then used as input data for the Matpower model in simulation mode. The values generated for active/reactive power transmitted, active/reactive power in branches, voltage levels and phase angles obtained from LOPF and Matpower are compared in Table 4 using root mean square error (RMSE) and the Normalized RMSE (NRMSE).

These minor NRMSE and values confirm the high level of accuracy of the linearized model.

Table 3
Investment and operation costs (Statistics | Eurostat, 2021).

Production type	Operational cost ($/MWh fuel)	Investment cost	O & M cost ($/MW/yr)
PV	$C^{pv} = 0$	$I^{pv} = 178$ ($/m^2)	$O^{pv} = 8000$
WT	$C^{wt} = 0$	$I^{wt} = 997\,000$ $/MW	$O^{wt} = 33\,000$
CG	$C^{cg,p}, C^{cg,q} = 36$	0 (already installed)	$O^{cg} = 105\,00$
VG	$C^{vg,p}, C^{vg,q} = 10^{9}$ [a]	0	0

[a]This cost ensures that virtual generators are excluded as much as possible.
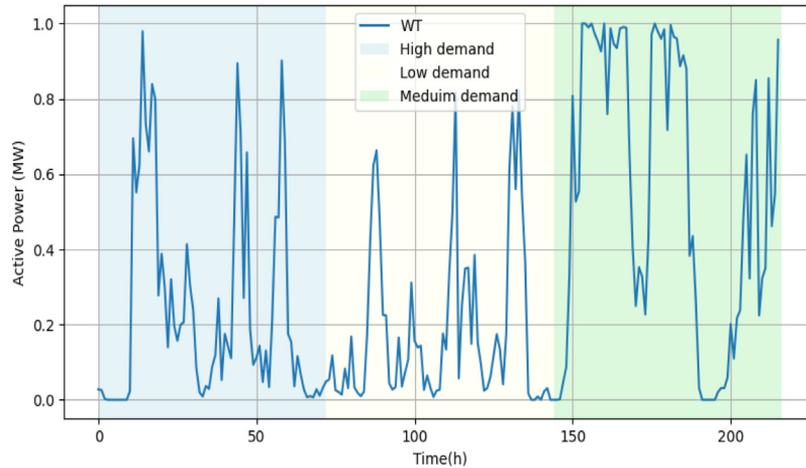
Fig. 5. Profile of one WT for nine typical days from three seasons (high = winter, low = summer, medium = spring).

Table 4
LOPF Vs. Matpower (RMSE values).

Parameters	RMSE (LOPF-Matpower)	NRMSE
P	0 kW	0
Q	1.02 kVAr	0.03
P_{ij}	0.22 kW	0.04
Q_{ij}	1.5 kVAr	0.28
θ	4.61 degree	4.6
V	0.0089 V	0.00268

4.2. Mono-objective optimization results

Considering the case study illustrated in Fig. 2 in the case where the network is overloaded. In this case, existing sources are insufficient to meet the demand in some periods during the operation of the network. This is particularly the case in some peri-urban areas undergoing urban densification.

The LCOE optimization is performed on two cases to showcase the effect of integrating RES and BES to the network:

* Case 1: LCOE optimization without RES and BES integration by considering only CGs and VGs. Thanks to the existence of VGs the DLOPF will systematically converge to an optimal solution by using generated power from VGs when the installed capacity of CGs is insufficient or when the network's constraints prevent electricity supply to some consumers. The PSO part of the model is not used in this case since there is no BES to be sized.

* Case 2: LCOE optimization with RES and BES integration where the bilevel PSO-DLOPF outlined in Fig. 1 is used on the same case network to determine the optimal placement and sizing of RES and BES while respecting all the network's constraints.

4.2.1. Energy management results

Fig. 6 shows optimal power generation by two CGs (1 and 2) and one VG (21) for the nine typical days and for both case 1 (Fig. 6a, b, c) and case 2 (Fig. 6d, e, f).

For case 1, the active power generated by the CGs shows coherent profiles between generated power (Fig. 6a and b) and load (Fig. 3). The results show that in periods of high demand (between 4 am and 10 pm in Fig. 3) there was high usage of the generators (the same period is used in Fig. 6). In periods of low consumption (between 100 h and 110 h in Fig. 3), there was less usage of the CGs and the VGs were not used at all. For medium demand, there was low usage of the VGs (between 5 h and 10 h in bus 21, Fig. 6-c). Note also in Fig. 6-a,b that the generators were not used equally even though the production cost was equivalent for all generators. This is the direct effect of network constraints (Table 2), handled by the model.

In terms of the overall network, the total installed generation capacity of the CGs is 180 MW, i.e., greater than the cumulated maximum power at each bus, which is 90 MW (Fig. 3). Despite these conditions, production is not sufficient to meet demand. The deficits are shown in the form of power generated by virtual generators (e.g., bus 21, Fig. 6-c). In this case, the model demonstrates the limitations of the electrical grid occasioned by the allowable ranges of other optimization variables (voltage, phase angle, apparent power in branches, etc.), i.e., the network constraints. This also happens in other nodes of the network (not shown here). The difference in level of power production between the CGs not at maximum production capacity confirms that power is limited by the transmission capacity of the grid. The model reveals the achievable performance of a network with constraints and supply–demand units.

4.2.2. Energy planning results

The results of the PSO-DLOPF approach are presented in this section; these focus on minimization of investment and operating costs only; carbon emissions are not considered. To confirm the effectiveness of the proposed PSO-DLOPF model, two sets of results are compared in Table 5.

In case 2 above, Table 6 shows that the optimum corresponds to an installation of 13 wind turbines in three of the candidate buses (16, 19 and 30); the investment in solar energy PV is limited
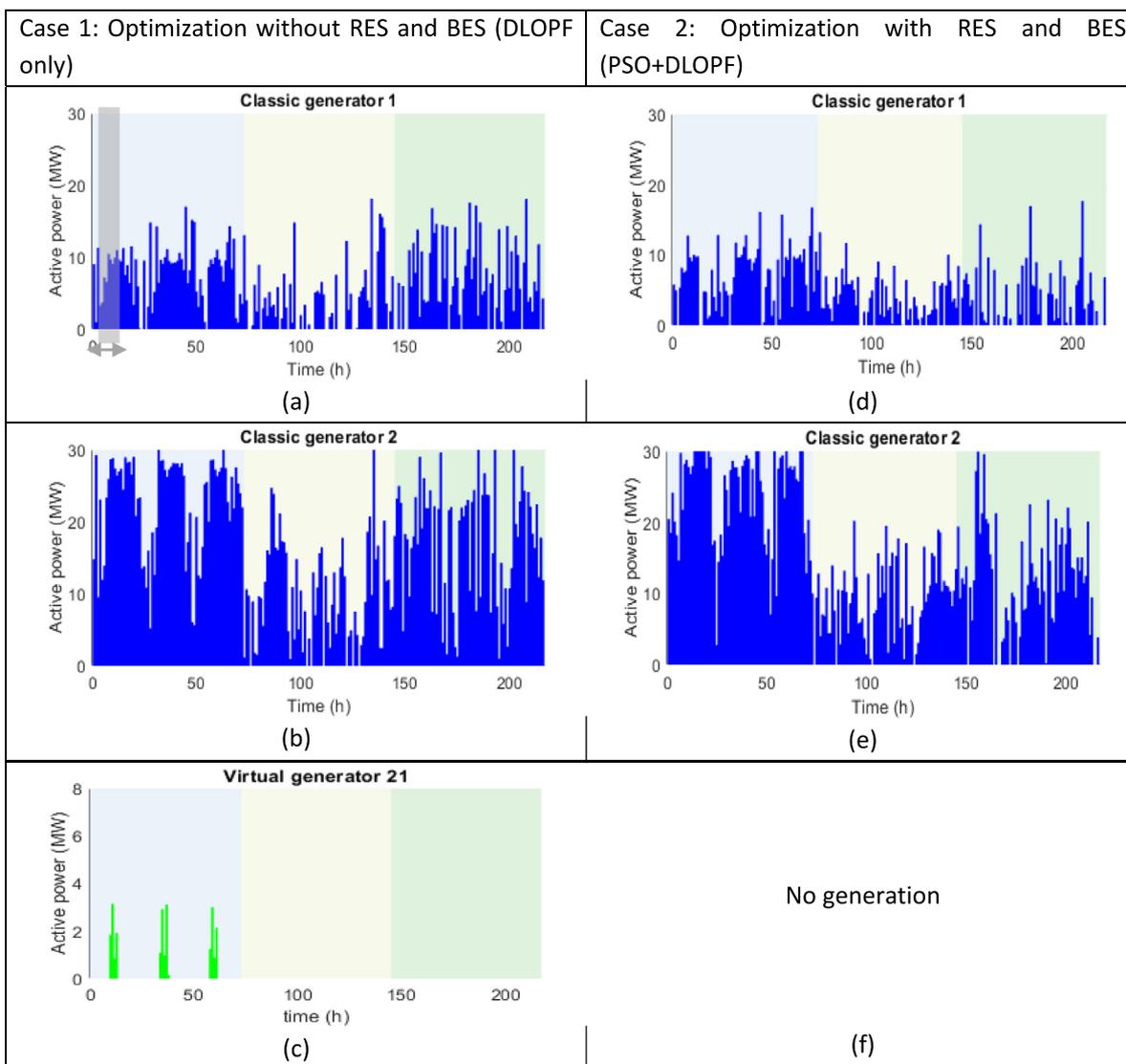
Case 1: Optimization without RES and BES (DLOPF only)	Case 2: Optimization with RES and BES (PSO+DLOPF)

Fig. 6. Active and virtual generated powers for some buses.

Table 5

Optimization results.

Energy supply over 9 days (MWh)	Case 1	Case 2
CG	12 131	11 359
VG	23.26	0
WT	–	738.05
PV	–	258.58
Total	12 154.6	12 355.6
Loss (%)	0.05	1.6

Table 6

Final optimal plan.

Bus number (case 2)	12	16	18	19	20	26	30
WT (W)	–	7	–	4	–	–	2
PV (A_p) $\ast 10^4$ (m^2)	–	–	–	–	2.7	–	1.5
BES (P^b) (MW)	5.33	–	7.16	4.26	–	7.64	
BES (D^T) (h)	4.9	–	7.02	5.84	–	3.14	

to buses 20 and 30. With these additional production sources (WTs and PVs), the reduction of classic production extraction shown in Fig. 6-d and -e (compared respectively with Fig. 6-a and -b) is justified, especially for medium demand.

Figs. 7 and 8 give a summary of the energy produced, showing the energy extracted from the available energy in each bus. The bar graph shows the energy extracted from the available energy resources (existing CGs, available surfaces for PVs and WTs) compared to the optimization results of the PSO-DLOPF to satisfy demand, taking grid constraints into account. The percentage of energy extracted from CGs is reduced by 6.5% (Table 5) and the remaining energy is extracted from WTs (5.97%) and PVs (2.09%). The penetration rate of renewables is therefore significant, reducing dependence on CGs and therefore the need for VGs. The total power produced in both cases is greater than the demand; the differences correspond to the losses along the network. In the second case, these losses were greater (1.6% more than case 1). This is due to the interconnection between the different buses in the network; although the positioning selected is considered optimal in terms of price, there are still losses along the lines due power being transmitted from some buses and stored in others (batteries are not necessarily located on the buses containing the generators). The loss rate is considered minimal in this case.

In terms of BES, the proposed optimization method places them in buses whether they contain producers, e.g., bus 19, or not, e.g., buses 12, 18 and 26. The production/storage behavior is illustrated in Figs. 9 and 10.
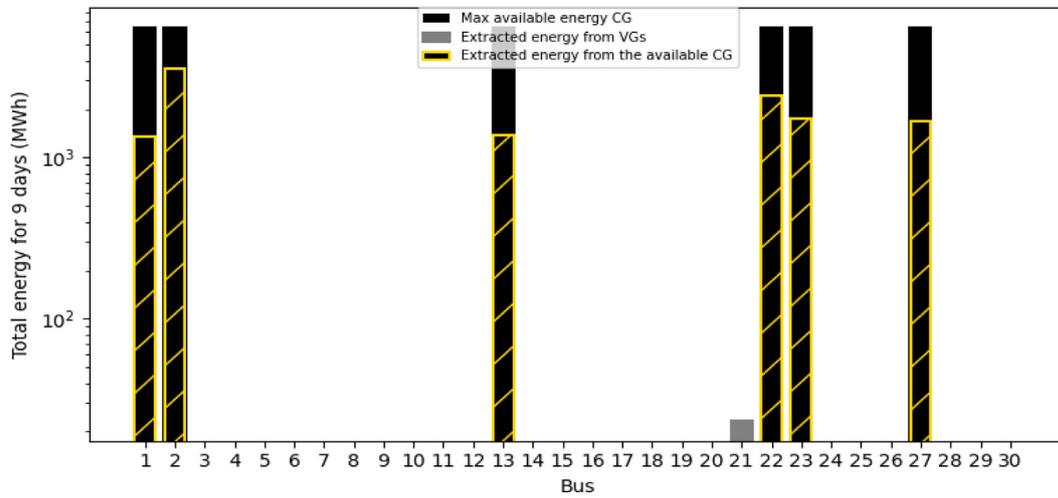
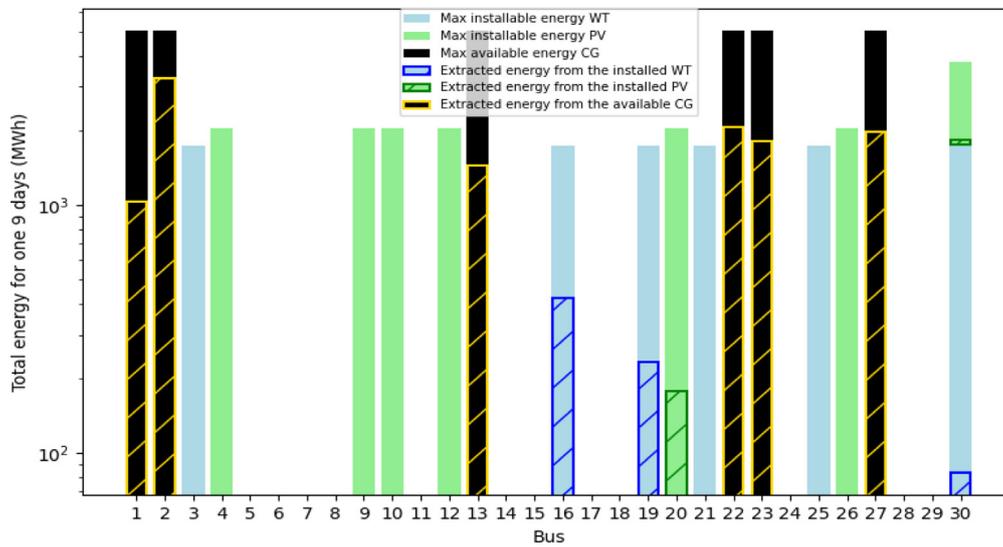**Fig. 7.** Use of energy resources on different buses (case 1).

Fig. 8. Use of energy resources on different buses (case 2).
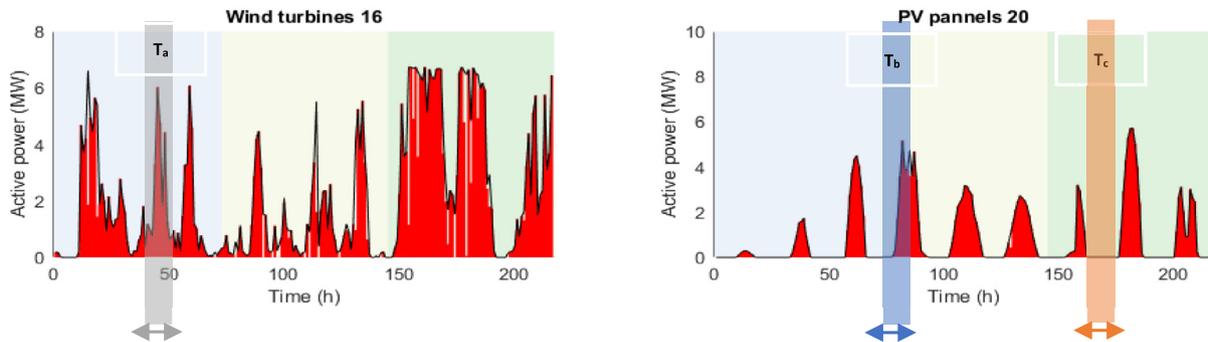

Fig. 9. Results of WT production, buses 19 and 26.

Fig. 9 shows the use of the installed renewable sources (red area) compared to their maximum production capacity (plotted black curve). These resources are intermittent and dependent on weather conditions. All the installed power is extracted from the PVs at bus 20 (illustrative example) and 95% from the installed power is extracted from the WTs of bus 16. Maximum solicitation of the WTs and PVs is observed compared to their maximum

installed capacity power (the load[1] factor of the WTs at bus 16 is 95% and 99% for the PVs at bus 26).

A comparison of Figs. 9 and 10 shows a synchronous charging and discharging depending on the local WT production (T_a: bus

---

[1] The load factor is calculating by dividing the sum of extracted power (red plots) by the installed power (black curve profile).
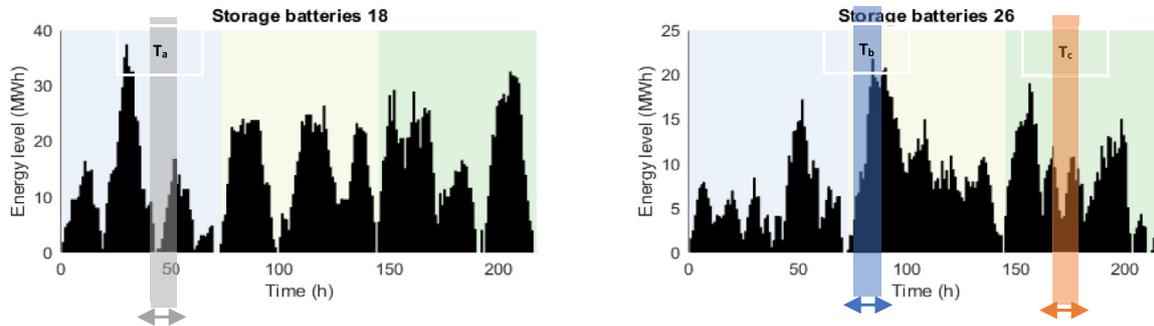
Fig. 10. Storage batteries, buses 19 and 26 (case 2).

Table 7
Final optimal costs.

Associated costs over 30 yr ($m)	Case 1	Case 2
PV inv. Cost	–	4.47
WT inv. cost	–	15.5
BES inv. cost	–	17.4
CG inv. cost	55 ($1.1 m/MW Statistics | Eurostat, 2021)	–
PV O&M cost	–	2.66
WT O&M cost	–	12.87
CG O&M cost	72.45	56.7
CGs op. cost	532.3	497.46
Total	659.7	644.9
Total reduction amount (%)		2.25%

Table 8
RES portion by scenario.

Abatement Ta (%)	CO2 emissions (gCO$_2$/yr)	RES production share (%)
∅ (No limit)	$2.2e^{10}$	8
70	$1.68e^{10}$	30
55	$1.297e^{10}$	46
40	$9.127e^{9}$	62
30	$7.2e^{9}$	70.10

16 between 45 h and 50 h or T_b: bus 20 between 75 h and 80 h), where the BES are charged then discharged afterwards. In this case, the storage batteries are charged directly from the RES on the nearest buses. Since some charging and discharging phases are not synchronous with RES production (T_c: bus 20 between 160 h and 170 h), it can be concluded that optimal storage also serves the network as a whole and this stored energy is imported from the power injected by different producers into the network. The total stored energy will be discharged and injected into the grid (see Table 7).

Integrating RES and BES into the grid is not inexpensive considering the estimated real investment and O&M costs ($109.6 m) as detailed in Fig. 4, but it reduces the production cost by 4.8% due to the decrease in CG production. This contributes to a 2.25% reduction in cost, compared to case 1, over the lifetime of both RES and BES. In this case, the production deficit (energy produced by virtual generators) should be extracted from an installed 50 MW combined cycle power plant (CCGT).

4.3. Bi-objective application results of PSO-DLOPF

4.3.1. Renewables, costs and emissions analysis

To illustrate the potential of the PSO-DLOPF in a bi-objective model, CO$_2$ emission constraints (Ta) are included in the problem, with different values in four different scenarios as presented in the first column of Table 8. This bi-objective approach leads to a Pareto distribution. Following the ε-constraint method (Mavromatidis et al., 2018), the Eq. (22) is used. The CO2 emitted by 1 MWh of CG power is $En^{cg} = 48\,000$ g CO$_2$/MWh (EDF, 2022). In each scenario, the ε-constraint Ta is chosen relative to the amount of CO$_2$ emitted in the first case (Table 8) so Ta is the

percentage of admissible amount of CO$_2$ emissions compared to the first scenarios (reference case without CO$_2$ constraint). In this Table 8, it can be seen that the RES portion follows exactly the same trend as the CO2 abatement rate. The amount of CO2 emissions decreases from $2.2e^{10}$ gCO2/yr to $7.2e^{9}$gCO$_2$/yr which is due to the increase in RES share from 8% to 70%. In the last 4 cases, the optimization is heavily influenced by the emission constraint. In contrast, for the first case where there are no CO$_2$ emissions to limit the CG, power extraction is only influenced by cost minimization which, explains the 8% portion of RES. Fig. 11 shows the extraction rate of renewable energy invested in the corresponding nodes following a high CO$_2$ emission requirement ($Ta = 30\%$). The figure shows that almost 75% of the available energy is used to produce zero-emission renewable energy.

Reducing CO$_2$ emissions means an increase in the total investment cost (Fig. 12). Using less power from classic generators therefore requires the installation of more RES and BES. This justifies the cost increase (from $75.2 m to $353 m, +371%). However, the total cost (investment + O&M + operation) increases (from $645 m to $660 m, +2,3%) with the reduction in CO$_2$ emissions resulting from limited use of CGs, as shown in Fig. 13. Consequently, as stricter emission constraints are imposed, the total cost increases; a 62% reduction in CO$_2$ emissions compared to the first case entails a 2.3% increase in costs at the scale considered.

4.3.2. BES analysis

To design a BES, the maximum power and duration must be defined. The maximum power ($P_{i^b}^b$) and storage duration (D_{i^b}) distributions are shown as bar plots in Fig. 14. These factors increase in average until they reach the upper bounds (3) for $Ta = 30\%$, where the BES are most needed to recover production. The product of these two factors (D_{i^b} and $P_{i^b}^b$) gives the size of the BES in terms of maximum energy (E^b), as in Fig. 15. The maximum energy storage increases and the BES increases in size with the reduction in CO$_2$ emissions. With the constraint $Ta = 30\%$, the upper limits are achieved approximately (64 MWh), which means that the BES investment limit is already covered.
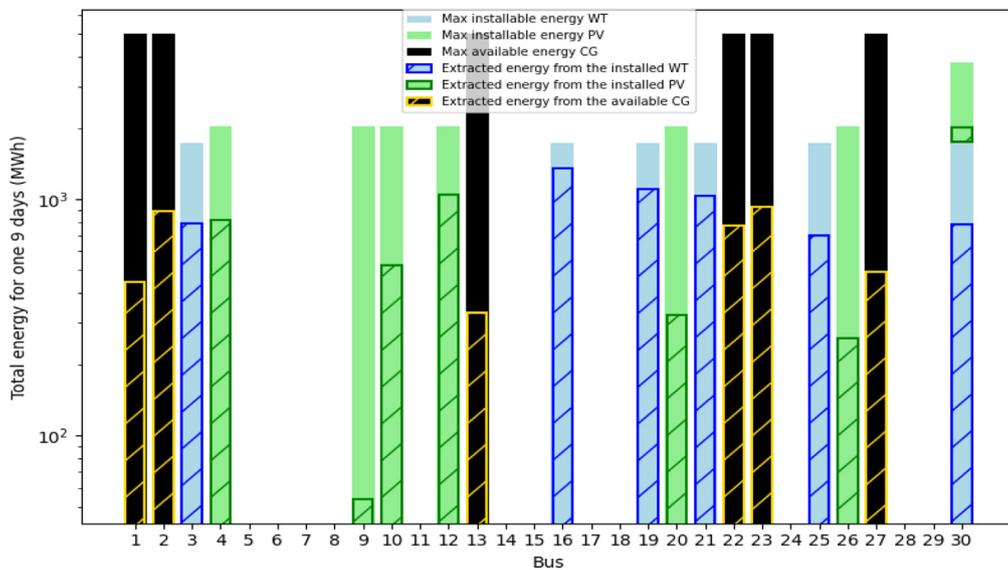
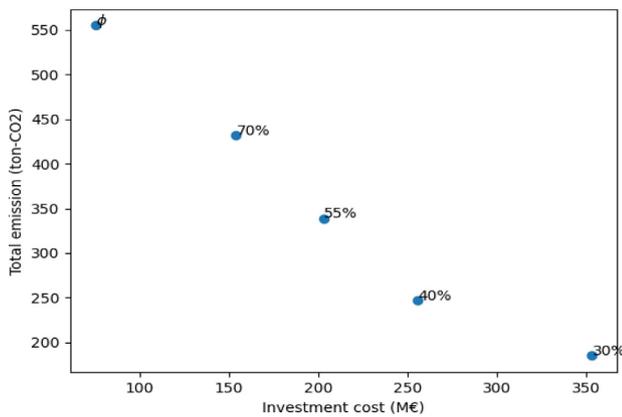**Fig. 11.** Use of energy resources at different buses (Ta = 30%).

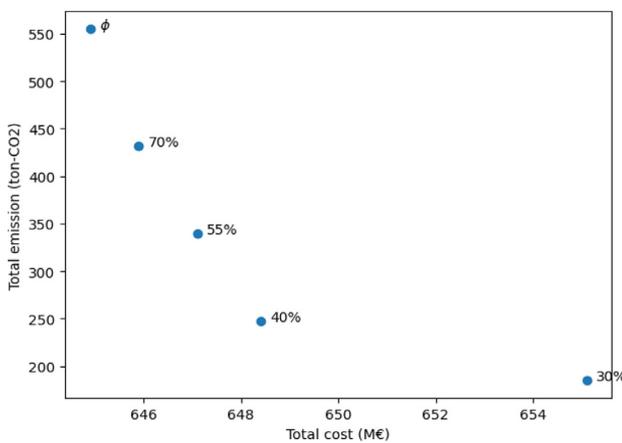**Fig. 12.** CO_2 emissions in terms of total investment cost.

Fig. 13. Evolution of bi-objective functions.

In some cases, the BES are located where the RESs are installed (e.g., bus 19 in ∅). BES are never placed where there are CGs. By designing smaller batteries (*no limits*), the charging rate is greater than for large batteries (*Ta* = 30%). With this charge rate (mean

= 32%) in the largest possible batteries (*Ta* = 30%) the emissions limit would be improved (≤ −70%).

5. Conclusion and perspective

In this study, a bi-level PSO-DLOPF approach was developed for energy planning in transmission networks. The cost minimization problem was split into upper and lower-level optimization models. In the upper level, a PSO was used to locate and size the BES. In the lower-level, an adapted DLOPF model was used to maximize the portion of RES, in order to identify the optimal size and location of RES and dispatch of energy production and storage dispatch in observance of carbon emissions constraints. The principle of virtual generators was introduced to guarantee a solution in view of the increasing power consumption with a limited grid, in terms of branch capacities, voltages and phase angles. The model reflects actual network behavior under specific constraints and ensures an optimal solution over a defined period constituted of nine typical days selected using a k-mean clustering approach. In addition, it enabled visualization of the dynamic behavior of the various parameters and optimization variables for each bus and in each branch. This bi-level model demonstrates the importance of storage and its design in terms of battery specifications.

The optimization model is used to perform a bi-objective optimization with respect to an economic criterion (LCOE) and an environmental criterion (CO_2 emission). Results show that the transition to a 30% CO_2 emissions limit increases the investment costs by +371%, the total costs by 2.3% and thus leads to a saturation of the storage capacity. it is therefore not possible to decrease beyond 30% despite the presence of installable RES capacities. It is not possible to install more RES because of network constraints.

The work can be extended in various ways: the model can support the decision-making process (energy planning) by introducing additional characteristics to remove or maintain local producers; it could also be coordinated with demand-side management models.

CRediT authorship contribution statement

Sara Fakih: Conceptualization, Methodology, Software, Writing – original draft, Writing – review & editing. **Mohamed Tahar**
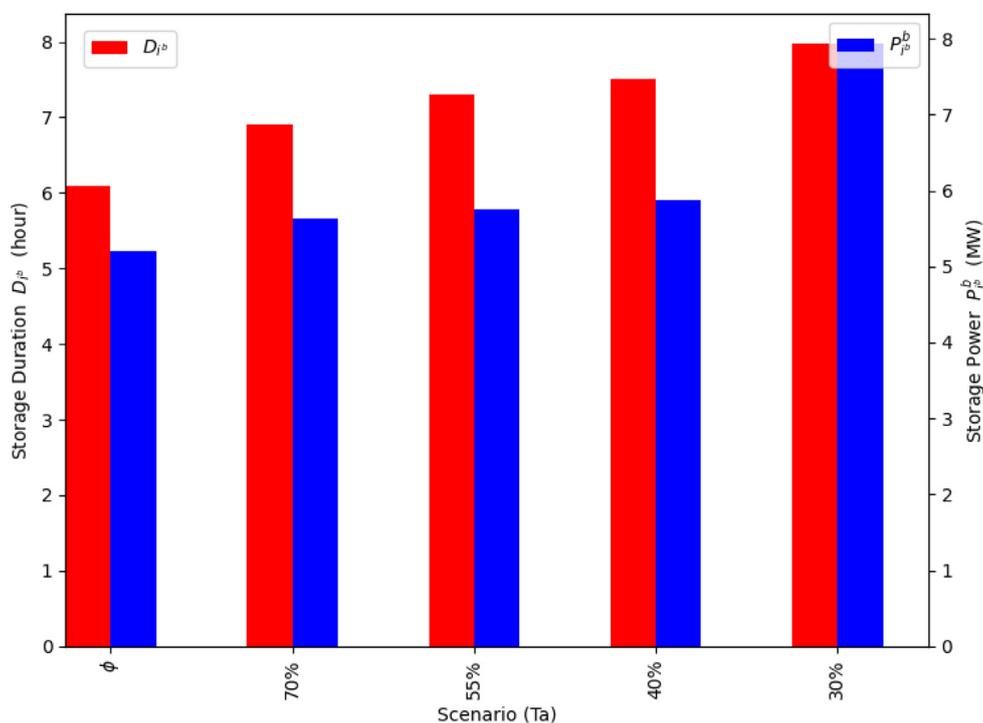
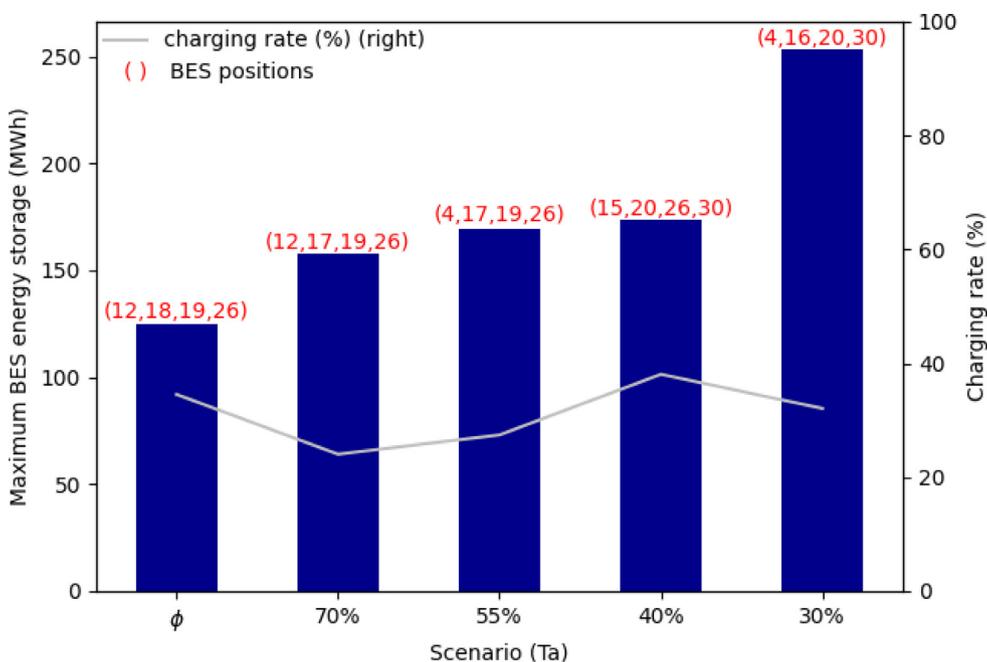**Fig. 14.** Bar plots for BES maximum storage power and storage length for each scenario (MW).

Fig. 15. Maximum energy storage for each scenario (MWh).

Declaration of competing interest

The authors declare that they have no known competing financial interests or personal relationships that could have appeared to influence the work reported in this paper.

Data availability

No data was used for the research described in the article

Acknowledgments

References

Akbari, T., Tavakoli Bina, M., 2016. Linear approximated formulation of AC optimal power flow using binary discretisation. IET Gener. Transm. Distrib. 10, 1117–1123. http://dx.doi.org/10.1049/iet-gtd.2015.0388.

Ali, E.S., Abd Elazim, S.M., Abdelaziz, A.Y., 2017. Ant lion optimization algorithm for optimal location and sizing of renewable distributed generations. Renew. Energy 101, 1311–1324. http://dx.doi.org/10.1016/j.renene.2016.09.023.

Alshammari, N., Asumadu, J., 2020. Optimum unit sizing of hybrid renewable energy system utilizing harmony search, jaya and particle swarm optimization algorithms. Sustain. Cities Soc. 60, 102255. http://dx.doi.org/10.1016/j.scs.2020.102255.

AlSkaif, T., Luna, A.C., Zapata, M.G., Guerrero, J.M., Bellalta, B., 2017. Reputation-based joint scheduling of households appliances and storage in a microgrid with a shared battery. Energy Build. 138, 228–239. http://dx.doi.org/10.1016/j.enbuild.2016.12.050.

Amigue, F.F., Essiane, S.N., Ngoffe, S.P., Ondoa, G.A., Mengounou, G.M., Nna Nna, P.T., 2021. Optimal integration of photovoltaic power into the electricity network using slime mould algorithms: Application to the interconnected grid in north Cameroon. Energy Rep. 7, 6292–6307. http://dx.doi.org/10.1016/j.egyr.2021.09.077.

Arabi-Nowdeh, S., Nasri, S., Saftjani, P.B., Naderipour, A., Abdul-Malek, Z., Kamyab, H., Jafar-Nowdeh, A., 2021. Multi-criteria optimal design of hybrid clean energy system with battery storage considering off- and on-grid application. J. Clean. Prod. 290, 125808. http://dx.doi.org/10.1016/j.jclepro.2021.125808.

Azizipanah-Abarghooee, R., Terzija, V., Golestaneh, F., Roosta, A., 2016. Multiobjective dynamic optimal power flow considering fuzzy-based smart utilization of mobile electric vehicles. IEEE Trans. Ind. Inform. 12, 12.

Bartels, R.H., Golub, G.H., 1969. The simplex method of linear programming using LU decomposition. Commun. ACM 12, 266–268. http://dx.doi.org/10.1145/362946.362974.

Bayram, I.S., Abdallah, M., Tajer, A., Qaraqe, K.A., 2017. A stochastic sizing approach for sharing-based energy storage applications. IEEE Trans. Smart Grid 8, 1075–1084. http://dx.doi.org/10.1109/TSG.2015.2466078.

Biswas, P.P., Suganthan, P.N., Amaratunga, G.A.J., 2017. Optimal power flow solutions incorporating stochastic wind and solar power. Energy Convers. Manage. 148, 1194–1207. http://dx.doi.org/10.1016/j.enconman.2017.06.071.

Chung, C.Y., Yan, W., Liu, F., 2011. Decomposed predictor-corrector interior point method for dynamic optimal power flow. IEEE Trans. Power Syst. 26, 1030–1039. http://dx.doi.org/10.1109/TPWRS.2010.2080326.

Cole, W., Frazier, A.W., Augustine, C., 2021. Cost projections for utility-scale battery storage: 2021 update. Renew. Energy 21.

EDF, 2022. edf-urd-rapport-financier-annuel-2021-fr-v2.pdf.

Fakih, S., Mabrouk, M.T., Batton-Hubert, M., Lacarriere, B., 2022. Optimal allocation and sizing of renewable energy sources and storage systems to support over-solicited electricity grid. In: 2022 6th International Conference on Green Energy and Applications (ICGEA). Presented at the 2022 6th International Conference on Green Energy and Applications. ICGEA, IEEE, Singapore, Singapore, pp. 14–21. http://dx.doi.org/10.1109/ICGEA54406.2022.9791941.

Flagship report, iea, 2022. Global energy review: CO2 emissions in 2021.

Gabash, A., Li, P., 2012. Active-reactive optimal power flow in distribution networks with embedded generation and battery storage. IEEE Trans. Power Syst. 27, 2026–2035. http://dx.doi.org/10.1109/TPWRS.2012.2187315.

García-Muñoz, F., Díaz-González, F., Corchero, C., 2021. A novel algorithm based on the combination of AC-OPF and GA for the optimal sizing and location of DERs into distribution networks. Sustain. Energy Grids Netw. 27, 100497. http://dx.doi.org/10.1016/j.segan.2021.100497.

Gill, S., Kockar, I., Ault, G.W., 2014. Dynamic optimal power flow for active distribution networks. IEEE Trans. Power Syst. 29, 121–131. http://dx.doi.org/10.1109/TPWRS.2013.2279263.

Gonzalez-Longatt, Dr. Francisco M., 2010. IEEE 30 bus test system [WWW document]. URL https://fglongatt.org/OLD/Test_Case_IEEE_30.html (accessed 4.19.23).

Haiyan Chen, Jinfu Chen, Xianzhong Duan, 2005. Multi-stage dynamic optimal power flow in wind power integrated system. In: 2005 IEEE/PES Transmission & Distribution Conference & Exposition: Asia and Pacific. Presented at the 2005 IEEE/PES Transmission & Distribution Conference & Exposition: Asia and Pacific. IEEE, Dalian, China, pp. 1–5. http://dx.doi.org/10.1109/TDC.2005.1546979.

Hannan, M.A., Wali, S.B., Ker, P.J., Rahman, M.S.A., Mansor, M., Ramachandaramurthy, V.K., Muttaqi, K.M., Mahlia, T.M.I., Dong, Z.Y., 2021. Battery energy-storage system: A review of technologies, optimization objectives, constraints, approaches, and outstanding issues. J. Energy Storage 42, 103023. http://dx.doi.org/10.1016/j.est.2021.103023.

HelioScope | Commercial Solar Software [WWW Document], 2022. HelioScope. URL https://helioscope.aurorasolar.com/ (accessed 4.19.23).

HOMER Pro, 2022. [WWW Document]. URL https://www.homerenergy.com/products/pro/index.html (accessed 4.19.23).

Hota, P.K., Naik, A.P., 2016. Analytical review of power flow tracing in deregulated power system. Amer. J. Electr. Electron. Eng..

IEA, 2019. World energy report.

IRENA, 2022. Energy planning support [WWW document]. URL https://www.irena.org/energytransition/Energy-Planning-Support.

Jorgenson, J., Frazier, A.W., Denholm, P., Blair, N., 2022. Storage futures study: Grid operational impacts of widespread storage deployment (no. nrel/tp-6a40-80688, 1840718, mainid:77472). http://dx.doi.org/10.2172/1840718.

Kargarian, A., Mohammadi, J., Guo, J., Chakrabarti, S., Barati, M., Hug, G., Kar, S., Baldick, R., 2018. Toward distributed/decentralized DC optimal power flow implementation in future electric power systems. IEEE Trans. Smart Grid 9, 2574–2594. http://dx.doi.org/10.1109/TSG.2016.2614904.

Keck, F., Jütte, S., Lenzen, M., Li, M., 2022. Assessment of two optimisation methods for renewable energy capacity expansion planning. Appl. Energy 306, 117988. http://dx.doi.org/10.1016/j.apenergy.2021.117988.

Khan, I.U., Javaid, N., Gamage, K.A.A., Taylor, C.J., Baig, S., Ma, X., 2020. Heuristic algorithm based optimal power flow model incorporating stochastic renewable energy sources. IEEE Access 8, 148622–148643. http://dx.doi.org/10.1109/ACCESS.2020.3015473.

Kristiansen, T., 2003. Utilizing MATPOWER in optimal power flow. MIC 24, 49–59. http://dx.doi.org/10.4173/mic.2003.1.5.

Lamadrid, A.J., Mount, T.D., Thomas, R.J., 2011. Scheduling of energy storage systems with geographically distributed renewables. In: 2011 IEEE Ninth International Symposium on Parallel and Distributed Processing with Applications Workshops. Presented at the 2011 IEEE 9th International Symposium on Parallel and Distributed Processing with Applications Workshops. ISPAW, IEEE, Busan, Korea (South), pp. 85–90. http://dx.doi.org/10.1109/ISPAW.2011.49.

Li, B., Li, J., 2021. Probabilistic sizing of a low-carbon emission power system considering HVDC transmission and microgrid clusters. Appl. Energy 304, 117760. http://dx.doi.org/10.1016/j.apenergy.2021.117760.

Li, J., Liu, Z., Wang, X., 2022. Public charging station localization and route planning of electric vehicles considering the operational strategy: A bi-level optimizing approach. Sustainable Cities Soc. 87, 104153. http://dx.doi.org/10.1016/j.scs.2022.104153.

Li, J., Zhang, R., Wang, H., Liu, Z., Lai, H., Zhang, Y., 2021. Deep reinforcement learning for optimal power flow with renewables using spatial-temporal graph information. arXiv:2112.11461 [cs, eess].

Lian, J., Zhang, Y., Ma, C., Yang, Y., Chaima, E., 2019. A review on recent sizing methodologies of hybrid renewable energy systems. Energy Convers. Manage. 199, 112027. http://dx.doi.org/10.1016/j.enconman.2019.112027.

Ma, M., Huang, H., Song, X., Peña-Mora, F., Zhang, Z., Chen, J., 2022. Optimal sizing and operations of shared energy storage systems in distribution networks: A bi-level programming approach. Appl. Energy 307, 118170. http://dx.doi.org/10.1016/j.apenergy.2021.118170.

Maffei, A., Meola, D., Marafioti, G., Palmieri, G., Iannelli, L., Mathisen, G., Bjerkan, E., Glielmo, L., 2014. Optimal power flow model with energy storage, an extension towards large integration of renewable energy sources. IFAC Proc. Vol. 47, 9456–9461. http://dx.doi.org/10.3182/20140824-6-ZA-1003.01983.

Maiz, S., Baringo, L., García-Bertrand, R., 2022. Expansion planning of a price-maker virtual power plant in energy and reserve markets. Sustain. Energy Grids Netw. 32, 100832. http://dx.doi.org/10.1016/j.segan.2022.100832.

Maleki, A., Khajeh, M.G., Ameri, M., 2016. Optimal sizing of a grid independent hybrid renewable energy system incorporating resource uncertainty, and load uncertainty. Int. J. Electr. Power Energy Syst. 83, 514–524. http://dx.doi.org/10.1016/j.ijepes.2016.04.008.

Mavromatidis, G., Orehounig, K., Carmeliet, J., 2018. Uncertainty and global sensitivity analysis for the optimal design of distributed energy systems. Appl. Energy 214, 219–238. http://dx.doi.org/10.1016/j.apenergy.2018.01.062.

Morstyn, T., Hredzak, B., Agelidis, V.G., 2016. Dynamic optimal power flow for DC microgrids with distributed battery energy storage systems. In: 2016 IEEE Energy Conversion Congress and Exposition (ECCE). Presented at the 2016 IEEE Energy Conversion Congress and Exposition. ECCE, IEEE, Milwaukee, WI, USA, pp. 1–6. http://dx.doi.org/10.1109/ECCE.2016.7855059.

Olabi, A.G., Onumaegbu, C., Wilberforce, T., Ramadan, M., Abdelkareem, M.A., Al-Alami, A.H., 2021. Critical review of energy storage systems. Energy 214, 118987. http://dx.doi.org/10.1016/j.energy.2020.118987.

Pereira, S., Ferreira, P., Vaz, A.I.F., 2016. Optimization modeling to support renewables integration in power systems. Renew. Sustain. Energy Rev. 55, 316–325. http://dx.doi.org/10.1016/j.rser.2015.10.116.

Ritchie, H., Roser, M., 2020. Our world in data.

Sadeghi, D., Hesami Naghshbandy, A., Bahramara, S., 2020. Optimal sizing of hybrid renewable energy systems in presence of electric vehicles using multi-objective particle swarm optimization. Energy 209, 118471. http://dx.doi.org/10.1016/j.energy.2020.118471.

Shaheen, M.A.M., Hasanien, H.M., Al-Durra, A., 2021a. Solving of optimal power flow problem including renewable energy resources using HEAP optimization algorithm. IEEE Access 9, 35846–35863. http://dx.doi.org/10.1109/ACCESS.2021.3059665.

Shaheen, M.A.M., Hasanien, H.M., Turky, R.A., Ćalasan, M., Zobaa, A.F., Abdel Aleem, S.H.E., 2021b. OPF of modern power systems comprising renewable energy sources using improved CHGS optimization algorithm. Energies 14, 6962. http://dx.doi.org/10.3390/en14216962.

Silva, E.G., 2018. Optimization of the planning and operations of electric distribution grids in the context of high renewable energy penetration.

Smale, S., 1983. On the average number of steps of the simplex method of linear programming. Math. Program. 27, 241–262. http://dx.doi.org/10.1007/BF02591902.

Statistics | Eurostat, 2021. [WWW Document]. URL https://ec.europa.eu/eurostat/databrowser/view/ten00118/default/table?lang=en (accessed 4.19.23).

Torrent-Fontbona, F., López, B., 2016. Decision support for grid-connected renewable energy generators planning. Energy 115, 577–590. http://dx.doi.org/10.1016/j.energy.2016.09.046.

Uturbey, W., Costa, A.S., 2003. Interruptible load management assessment via dynamic optimal power flow. In: 2003 IEEE Bologna Power Tech Conference Proceedings,. Presented at the 2003 IEEE Bologna Power Tech. IEEE, Bologna, Italy, pp. 588–594. http://dx.doi.org/10.1109/PTC.2003.1304787.

Walter Short, Packey, Daniel J., Thomas Holt, 1995. A manual for the economic evaluation of energy efficiency and renewable energy technologies.

World energy outlook 2019, 2019. International ebergy agency IEA.

Xu, X., Hu, W., Cao, D., Huang, Q., Chen, C., Chen, Z., 2020. Optimized sizing of a standalone PV-wind-hydropower station with pumped-storage installation hybrid energy system. Renew. Energy 147, 1418–1431. http://dx.doi.org/10.1016/j.renene.2019.09.099.

Yang, Z., Zhong, H., Xia, Q., Bose, A., Kang, C., 2016. Optimal power flow based on successive linear approximation of power flow equations. IET Gener. Transm. Distrib. 10, 3654–3662. http://dx.doi.org/10.1049/iet-gtd.2016.0547.

Yang, H., Zhou, W., Lu, L., Fang, Z., 2008. Optimal sizing method for stand-alone hybrid solar–wind system with LPSP technology by using genetic algorithm. Sol. Energy 82, 354–367. http://dx.doi.org/10.1016/j.solener.2007.08.005.

Zebarjadi, M., Askarzadeh, A., 2016. Optimization of a reliable grid-connected PV-based power plant with/without energy storage system by a heuristic approach. Sol. Energy 125, 12–21. http://dx.doi.org/10.1016/j.solener.2015.11.045.